HHS Public Access

Author manuscript

Phys Med Biol. Author manuscript; available in PMC 2019 February 26.

Published in final edited form as:

Phys Med Biol. ; 63(5): 05TR01. doi:10.1088/1361-6560/aaaca4.

MRI-only treatment planning: benefits and challenges

Amir M. Owrangi[*,1], **Peter B. Greer**[2,3], and **Carri K. Glide-Hurst**[4,5]

[1]Department of Radiation Oncology, UT Southwestern Medical Center, Dallas, Texas

[2]School of Mathematical and Physical Sciences, University of Newcastle, Newcastle, NSW, 2308, Australia

[3]Department of Radiation Oncology, Calvary Mater Hospital, Newcastle, NSW, 2298, Australia

[4]Department of Radiation Oncology, Henry Ford Health System, Detroit, Michigan

[5]Department of Radiation Oncology, Wayne State University School of Medicine, Detroit, Michigan

Abstract

Over the past decade, the application of magnetic resonance imaging (MRI) has increased, and there is growing evidence to suggest that improvements in the accuracy of target delineation in MRI-guided radiation therapy may improve clinical outcomes in a variety of cancer types. However, some considerations should be recognized including patient motion during image acquisition and geometric accuracy of images. Moreover, MR-compatible immobilization devices need to be used when acquiring images in the treatment position while minimizing patient motion during the scan time. Finally, synthetic CT images (i.e. electron density maps) and digitally reconstructed radiograph (DRR) images should be generated from MRI images for dose calculation and image guidance prior to treatment. A short review of the concepts and techniques that have been developed for implementation of MRI-only workflows in radiation therapy is provided in this document.

Keywords

MRI only radiation therapy; substitute CT; pseudo CT; synthetic CT; radiotherapy; treatment planning

1. Introduction

Treatment planning in modern radiation therapy procedures involves the use of both computed tomography (CT) and magnetic resonance imaging (MRI) for patients in many disease sites, with the former providing electron density values that are necessary for treatment planning, and the latter providing superior soft tissue contrast and for tumor and soft tissue delineation. Examples of soft tissue contrast superiority of MRI in comparison with CT for brain, prostate and cervical cancer are shown in Figures 1–3.

[*]**Corresponding author:** Amir Owrangi, PhD, DABR, Assistant Professor, Department of Radiation Oncology, UT Southwestern Medical Center, 2280 Inwood Rd, EC2.242, Dallas, TX 75235, Tel: (214) 648-8366, Fax: (214) 645-7389, maowrangi@gmail.com.

Delineating the gross tumor volume (GTV) has been called “the weakest link” in the chain of factors affecting radiotherapy accuracy(Njeh, 2008). Current computed tomography (CT) variability in GTV delineation introduces more error than daily setup uncertainties(van Mourik *et al.*, 2010; Van Herk, 2004; Weiss and Hess, 2003; Weiss *et al.*, 2003; Rasch *et al.*, 2005; Vorwerk *et al.*, 2009). In an era of intensity modulated radiation therapy, where steep dose gradients sculpt dose away from organs at risk (OARs), accurate delineation becomes of paramount importance to avoid geometric misses and prevent recurrences. Importantly, no level of on-board image guidance will eliminate these systematic delineation errors(Njeh, 2008). The consequences of these systematic uncertainties can be great; inadequate target coverage has been linked to significant reductions in tumor control(Kim *et al.*, 1995) and clear patterns of failure(Chen *et al.*, 2011).

Importantly, incorporating MRI in treatment planning significantly reduces inter- and intra-observer contouring variability for many disease sites(Jolicoeur *et al.*, 2011; Giezen *et al.*, 2012; Rasch *et al.*, 2005; Rasch *et al.*, 1999). In the brain, MRI can resolve tumor boundaries not resolvable on CT(Just *et al.*, 1991) and identifies peritumoral edema(Chang *et al.*, 2007). For prostate, MRI is extremely beneficial for accurately identifying the prostate, areas of high tumor burden, sensitive erectile tissues, and the prostatic apex, which cannot be identified on CT as suggested by ACR Appropriateness Criteria(Wachter *et al.*, 2002; Debois *et al.*, 1999; Rasch *et al.*, 1999; Hentschel *et al.*, 2011; Nguyen *et al.*, 2014). Accurate delineation of this region is critical: high tumor incidence occurs in the apical posterior region(Chen *et al.*, 1997). For female pelvis, RTOG consensus atlas states that MRI provides precise delineation of the uterus and cervix and identifies the superior/inferior bladder extent(Gay *et al.*, 2012). GEC ESTRO guidelines conclude that MRI provides the most reliable delineation for gynecological cancer(Pötter *et al.*, 2006).

The benefits of using MRI for delineation include improved dosimetry and the potential to increase the therapeutic ratio. Prostate delineation on MRI has enabled dose escalation of 2–7 Gy while maintaining the same rectal wall dose(Steenbakkers *et al.*, 2003). Likewise, an MRI-assisted dose volume escalation study for cervical cancer revealed ~10–20% survival gains while reducing gastrointestinal and urinary late morbidity(Pötter *et al.*, 2007).

Furthermore, MRI is a multi-parametric imaging modality that not only can provide anatomical information with high soft-tissue contrast, but also can provide valuable functional information that can be used for assessment of disease progression and treatment response evaluation(Khoo and Joon, 2006; Maikusa *et al.*, 2013). In brain, functional diffusion-weighted MRI images can be used to reliably evaluate treatment response at various time points during and post-treatment (Hamstra *et al.*, 2008; Mardor *et al.*, 2003). Functional information of surrounding normal structures can also be considered during treatment planning to improve target coverage while minimizing the dose to the adjacent functioning tissues (Garcia-Alvarez *et al.*, 2006; Kovacs *et al.*, 2011). Likewise in cervix, diffusion-weighted imaging has been considered as a potential tool for monitoring treatment response (Levy *et al.*, 2011; McVeigh *et al.*, 2008). In prostate, dynamic contrast enhanced (DCE) MRI scans can be used for detection and localization of recurrent prostate cancer after radiotherapy and such functional information can be helpful for planning of potential salvage treatment (Haider *et al.*, 2008). By incorporating functional information acquired

from MRI images, patients' quality of life has improved via minimizing the dose to the surrounding nerves, vessels and other normal structures without compromising target coverage (McLaughlin *et al.*, 2005).

Currently, the existing CT-based treatment planning workflow relies on target and OAR definition on MRI and a transfer of contours to CT via image registration. MRI-CT co-registration introduces geometrical uncertainties of ~2 mm for the brain(van Herk and Kooy, 1994; Ulin *et al.*, 2010) and 2–3 mm for prostate and gynecological patients(Wang and Doddrell, 2005). Importantly, these errors are systematic, persist throughout treatment, shift high dose regions away from the target(Van Herk, 2004) and could lead to a geometric miss that compromises tumor control. Recently, MRI-simulation platforms have emerged as attractive alternatives to CT-simulation(Devic, 2012; Kapanen *et al.*, 2012; Glide-Hurst *et al.*, 2015b; Paulson *et al.*, 2015). These differ from diagnostic MRI by including larger bore size, flat tabletops to accommodate immobilization devices, external laser systems, and dedicated imaging protocols. By acquiring MRI-simulation data in the treatment position, combined with modern low distortion techniques an accurate MRI-based anatomical patient model can be generated that minimizes the variation in patient positioning between the time of simulation and the time of treatment(Devic, 2012). This capability has recently led to the concept of MRI-only based treatment planning, where artificial or synthetic CT data for dose calculation is generated directly from the MRI scan. Many groups have shown a strong interest to move toward MRI-only treatment planning(Doemer *et al.*, 2015a; Glide-Hurst *et al.*, 2015b; Kim *et al.*, 2015c; Kim *et al.*, 2015b; Price *et al.*, 2015; Zheng *et al.*, 2015; McGee *et al.*, 2015; Kapanen *et al.*, 2013; Pötter *et al.*, 2007; Hsu *et al.*, 2013b; Hsu *et al.*, 2015b; Dowling *et al.*, 2012; Lambert *et al.*, 2011a; Rivest-Hénault *et al.*, 2015).

MRI-only treatment planning will reduce CT scanning (reducing radiation dose, patient time, and imaging costs), streamline clinical efficiency, and will fully exploit the benefits of MRI for high-precision treatment planning. It will enable more efficient uses of resources and a reduction in duplicated effort (i.e., between diagnostic radiology and radiation oncology). Importantly, MRI-only planning removes systematic CT-MRI registration uncertainties to facilitate improved geometric treatment accuracy. However there are several challenges to be overcome to introduce MRI-only planning into the clinic. These include the production of robust MRI-only patient models and synthetic CT scans with accurate geometry and electron densities.

The purpose of this article is to review the current state-of-the-art, including potential benefits and challenges remaining for MRI only treatment planning for external beam radiotherapy. We will also highlight unmet needs and future directions.

Artifacts and geometric distortions

Geometric distortions in MRI consist of two major components: system-level (arising from gradient nonlinearity (GNL) in the spatial encoding gradients(Baldwin *et al.*, 2007a; Chen *et al.*, 2004b) and B_0 field inhomogeneities) and patient-level (chemical shift artifacts and susceptibility)(Wang *et al.*, 2013). System-level distortions are magnet-specific and not sequence or object dependent. Currently, GNL distortion corrections are built into the MRI reconstruction software and have been shown to be the dominant source of geometric

distortion(Baldwin *et al.*, 2007c). In a perfect situation the main magnetic field is uniform and magnetic fields from gradients are linear; however, in reality the gradients are not perfect and gradient fields are non-linear. This non-linearity becomes more noticeable away from the scanner isocenter toward the edges of the scanner maximum field of view(Doran *et al.*, 2005; Price *et al.*, 2015; Wang and Doddrell, 2005). Thus, one approach to reducing the impact of GNL is to localize the object of interest as close to isocenter as possible. Geometric distortion not only occurs in the phase and readout encoding direction, it can also occur in the slice selection direction where the slice thicknesses may change as a function of position. To reduce the effect of GNL, one can increase the gradient amplitude, but at the same time the bandwidth needs also to be increased. However, increasing the radiofrequency (RF) receiver bandwidth reduces the signal to noise ratio (SNR) and increasing the RF transmitter bandwidth will increase the transmitting RF power and may go over the allowable specific absorption ratio (SAR). Having images with acceptable quality and high geometric integrity is necessary for radiotherapy treatment planning(Jovicich *et al.*, 2006; Tavares *et al.*, 2014) and therefore, all necessary steps need to be taken to minimize potential distortions in MRI images.

Another source of image distortion may arise from eddy currents that are generated by rapidly pulsed gradients. According to the Faraday-Lenz Law of electromagnetism, changing magnetic field induce electrical currents in nearby conductors. Since MRI uses rapidly changing gradient magnetic fields, eddy currents are always produced; however, the magnitude of eddy currents depends on the rate of change of the magnetic field. Therefore, fast imaging sequences such as echo-planar imaging, diffusion-weighted imaging and MR spectroscopy produce the largest and most severe eddy current problems. In earlier generation magnets with unshielded gradients, distortions up to 1.3 mm have been reported in a 1.5T cylindrical bore magnet(Tanner *et al.*, 2000). More modern hardware and shielded gradients have been shown to compensate for eddy currents, with distortion differences of <0.2 mm over several echo time settings reported for a 1.0 T Open MR-SIM (Price *et al.*, 2015) and <0.3 mm for a 3.0T cylindrical magnet(Baldwin *et al.*, 2007b).

Another method to reduce geometric distortion is to select pulse sequences with appropriate parameters. Sequences with fast gradient switching are more prone to gradient distortion and using them should be considered with caution. The other effective way of reducing system-related geometric distortion that have been described in literature(Caramanos *et al.*, 2010; Janke *et al.*, 2004; Maikusa *et al.*, 2013; Chen *et al.*, 2004b) is to apply distortion correction matrices before the final image is generated. This technique can be implemented once the distortion map of the MRI machine is characterized and it is currently included in the reconstruction for many MRI systems. It is important for the end-user to quantify the residual GNL (i.e. after vendor corrections) to determine if they are negligible, and if not, to understand their magnitude and location. If residual GNL after 3D distortion corrections is non-negligible, additional post-processing corrections can be implemented(Price *et al.*, 2015). Closed bore magnets have shown clinically acceptable GNL characterized within the clinically useable field of view (FOV) (Torfeh *et al.*, 2016; Huang *et al.*, 2016a). Thus, GNL needs to be measured for each magnet platform to deduce if further corrections are necessary before MRI-only radiotherapy is implemented. This can be done by using known test objects and phantoms with known landmarks, typically at a large field of view that at

least encompass the clinical scanning volumes (Caramanos *et al.*, 2010; Doran *et al.*, 2005; Sun *et al.*, 2015; Chen *et al.*, 2004b; Huang *et al.*, 2016b; Price *et al.*, 2017). MR images can then be compared to CT or a schematic of the expected phantom configuration as the gold standard.

Metal artifacts are one of the most common types of artifact in MRI images. These are due to susceptibility-related inhomogeneities in which metal-tissue or air-tissue interface in the presence of strong polarizing (B0) magnetic field will lead to strong susceptibility transitions which will be the source of large magnetic field distortions. Even though many implants are MRI safe, the artifacts induced by metal implants may distort the geometric integrity of the image and alter intensity values of the tissue voxels around the implant(Hargreaves *et al.*, 2011; McGee *et al.*, 2016; Schenck, 1996; Schmidt and Payne, 2015). For example metal artifact management is important for MRI-guided brachytherapy in which metallic objects, such as cervical applicators and titanium needles are used, which may adversely impact image quality and clinical usability(Hellebust *et al.*, 2010; Kirisits *et al.*, 2014; Tanderup *et al.*, 2008; Tanderup *et al.*, 2013; Tanderup *et al.*, 2014).

Some metal artefact reduction techniques are available although they may have limitations for radiation therapy purposes(Butts *et al.*, 2005; Choi *et al.*, 2015; Lu *et al.*, 2011; Reichert *et al.*, 2015). For example, some of these artefact reduction techniques have been developed for two-dimensional (2D) MRI images, whereas three-dimensional (3D) acquisition of MRI images and their use in radiation therapy planning are become more prevalent. Recently, advanced reconstruction methods for metal artifact reduction have been introduced that combine view-angle tilting (VAT) (Butts *et al.*, 2005; Choi *et al.*, 2015) and slice-encoding metal artifact correction (SEMAC)(Lu *et al.*, 2009). Other strategies include using spin-echo based pulse sequences instead of gradient echoes and increasing the receiver and excitation bandwidth. Since metal induced inhomogeneity of magnetic fields is much larger than tissue based inhomogeneity(Hargreaves *et al.*, 2011), these strategies may not completely eliminate artifacts. Some of the techniques applied by different vendors include imaging with high gradients and increased encoding to compensate the artefact in both in-plane and through-plane directions(Koch *et al.*, 2011; Koch *et al.*, 2009; Lu *et al.*, 2009). Figure 4 illustrates a case where a metal artifact correction technique was implemented in a patient with bilateral hip implants for both CT-simulation and MRI-simulation, highlighting the potential of mitigating metal artifacts while enabling the powerful soft tissue contrast of MRI to be utilized.

Patient-level distortions (B_0) are object and field-strength dependent, requiring patient-specific corrections. Effects resulting from susceptibility differences are most apparent near tissue/air interfaces due to local variations in the induced magnetic field and have been reported to be up to 4 mm at the sinus/tissue interface in the brain at 3.0T(Wang *et al.*, 2013). To measure these distortions, field maps, or a map of the off-resonance frequency at each voxel, are obtained. These are typically performed with a double-echo gradient echo based sequence and calculating the field map based on the difference in phase between two different echoes. Recently, Wang *et al.* performed repeat acquisition of field maps for 17 brain subjects and found a within-subject standard deviation of ~0.2 mm displacement in the frequency-encoding direction of 3D T1-weighted images (Wang *et al.*, 2013). Recent work

by Tyagi *et al.* evaluated patient-induced susceptibility distortion in the pelvis in 20 patients acquired at 3.0 T and measured the mean distortion within the prostate for a single time point as −0.2 mm (range: −0.62–0.35 mm) while the voxels within the body contour ranged from −0.73 to 0.56 mm(Tyagi *et al.*, 2016). While the overall magnitude of patient-specific distortions appears to be low, it can be further decreased by increasing the bandwidth. This suggests that anatomical site-specific recommendations may be advantageous. Overall, robust quantification and mitigation (either by increasing the bandwidth to minimize patient-specific distortions or developing a post-processing correction for system-level distortions), particularly for high precision MRI-only treatment planning, is imperative.

Production of synthetic CT

Unlike CT, electron densities of different tissues are not uniquely related to the image intensities in MRI. Therefore, direct mapping of MRI intensity to electron density using calibration phantoms cannot be used. However, several methods have been developed to estimate Hounsfield Units (HU) and hence electron density based on the intensity of MRI images. The estimation of HU is necessary as these are currently the input variable accepted by treatment planning systems, although in future systems electron density or tissue class/material may be more directly used. The HU map from MRI can therefore currently be considered as a scan from a “virtual” CT scanner. These mapping methods can be used for radiation therapy purposes and have also been developed for positron emission tomography (PET)-MRI scanner attenuation correction algorithms(Martinez-Möller and Nekolla, 2012; Zaidi *et al.*, 2003). Various terminologies have been used for the resulting synthetic CT including substitute CT, pseudo-CT, MRCAT and MRCT. The methods to generate synthetic CT images from MRI scans are classified here for clarity into: voxel based methods; atlas based methods; and hybrid methods. Systematic overviews of method types have recently been reported(Edmund and Nyholm, 2017; Johnstone *et al.*, 2017).

Voxel based methods use classification or calibration type approaches to determine the HU values from MRI data. These use a voxel by voxel mapping based on the intensity and/or spatial location of the MRI image voxel or combinations of intensities from different sequences.

Classification techniques separate MRI into discrete tissue classes and assign a bulk HU value to a voxel identified to belong to a particular class or a weighted average of HU values according to class probabilities. The simplest approach is to assume the patient is water-equivalent and assign a single density such as is done for conventional brachytherapy planning. This was introduced for MRI-only dose calculations for brain initially(Beavis *et al.*, 1998) and then for prostate(Chen *et al.*, 2004a; Chen *et al.*, 2004b). However it has been found that dose calculations are not clinically acceptable compared to heterogeneous density(Eilertsen *et al.*, 2008; Karotki *et al.*, 2011). The addition of a bone class improves dose calculation to mostly within 2% of the dose calculations on CT(Eilertsen *et al.*, 2008; Jonsson *et al.*, 2010; Karlsson *et al.*, 2009; Karotki *et al.*, 2011; Kim *et al.*, 2015a; Paradis *et al.*, 2015), falling within a range that has since been suggested as clinically acceptable(Korsholm *et al.*, 2014). For anatomical sites where air cavities are present the assignment of an air class will be required(Hsu *et al.*, 2015a). Separation of bone and air has

been performed with UTE pulse sequences (Catana *et al.*, 2010; Keereman *et al.*, 2010; Edmund *et al.*, 2014; Johansson *et al.*, 2011b; Johansson *et al.*, 2012; Robson *et al.*, 2003). Since bone has a very short T2*, using UTE pulse sequences can improve the contrast between bone and surrounding air or soft tissue. Fat and water classes can also be separated and segmented in MRI images acquired with Dixon pulse sequences, however whether this improves dose calculation accuracy significantly is unclear. Dixon uses the chemical shift difference between water and fat to separate the signals. Solutions in the pelvis have been proposed for combinations of T1-weighted, T2-weighted, and Balanced Turbo Field Echo (BTFE)(Kim *et al.*, 2015c) or T1-weighted and T2-weighted imaging(Kim *et al.*, 2015b). For the pelvis, image voxels were sorted into five material classifications: air, bone, fat, soft tissue, and fluid(Price *et al.*, 2015) and synthetic CT voxel assigned from a weighted sum of MRI voxel intensity and a class-dependent weighting factor. Fuzzy c-means clustering has been applied to the production of synthetic CT images of the head and neck(Hsu *et al.*, 2013a). A drawback of clustering techniques is that without reference to spatial position some tissues could be mislabeled. A closely related and simpler algorithm, k-means clustering, has been applied to other biomedical tasks including diagnosis of cirrhosis of the liver(Lee and Fujita, 2007).

Voxel based techniques have also been developed that apply regression or calibration formalisms to produce HU data. One method uses multiple MRI contrasts including UTE combined with gaussian mixture modelling regression(Johansson *et al.*, 2013). The major drawbacks are the requirement for multiple MRI sequences and prediction errors at tissue interfaces due to partial volume effects. Calibration techniques with single scan sequences have used separate mapping curves from MRI signal to HU for bone regions and soft-tissue regions(Korhonen *et al.*, 2014). This separation is required to obtain unique signal mappings and requires segmentation of bone regions on the acquired MRI scan. Extracting bone from MRI images is also useful for patient positioning(Nyholm and Jonsson, 2014). To enhance bone visibility a method has been developed that uses a single UTE type sequence with preliminary testing performed using porcine leg phantoms(Ghose *et al.*, 2017a). An interesting new approach is to generate synthetic CT scans using machine learning with convolution neural networks (CNN). A CNN approach using a single CT and dual-echo UTE sequence for training has been developed to transform MR intensity to CT using patches for PET-MRI attenuation correction(Roy *et al.*, 2017). Current deep learning methods require pairwise alignment of MR and CT training images of the same patient for MR-to-CT synthesis. Misalignment of these image pairs resulting in errors in synthetic CT. To overcome this problem a generative adversarial network (GAN) CNN method was recently developed using unpaired images and this was found to out-perform a GAN method with paired images(Wolterink *et al.*, 2017). Recent work by Han introduced a novel deep convolutional neural network (DCNN) method for synthetic CT generation in the brain(Han, 2017). Training was performed on 18 brain cancer patients with CT and T1-weighted MRI data in a six-fold cross-validation study yielding promising results: overall average MAE was ~84.8 ± 17.3 HU for all subjects.

In atlas-based methods, both single and multi-atlas techniques have been developed. The single atlas represents an average patient anatomy and is registered to the acquired MRI images using deformable image registration to produce an estimation of the HU. A CT atlas

can be used however this requires CT to MRI registration where the image signals are very different(Burgos *et al.*, 2013; Uh *et al.*, 2014). To overcome this problem a CT-MRI atlas-pair can be used where the CT and MRI atlas scan pair correspond anatomically(Dowling *et al.*, 2012). The MRI atlas scan is deformably registered to the acquired MRI image to derive deformation vectors that are then used to deform the conjugate CT atlas scan to produce the synthetic CT. The outcome of this method is dependent on how well the image registration can be performed which will depend on the differences in size and shape between the atlas and patient scans. A multi-atlas technique can similarly be performed to overcome the problem of variations in patient size and shape and the most similar atlas scan selected based on registration metrics. Applying image intensity and uniformity correction on the MRI images prior to CT-MRI image registration has been shown to improve image registration accuracy(Burgos *et al.*, 2013). It has also been shown that increasing the number CT cases that has been used to generate the atlas will improve the performance of atlas based registration(Uh *et al.*, 2014). The time to generate a synthetic CT using a multi-atlas approach has been quoted as at least 20 minutes using a Matlab with MEX code implementation of their algorithm(Farjam *et al.*, 2017).

Hybrid techniques combine atlas methods and voxel based approaches. A combination of atlas based deformable registration and local patch pattern recognition was proposed for brain MRI based attenuation correction(Hofmann *et al.*, 2008). An atlas database of MRI and CT scans was used with each MRI scan deformably registered to the acquired MRI scan. For a voxel in the acquired MRI the neighboring patches in the database scans are then found. A gaussian distributed predictive distribution for the voxel HU value is derived from the differences in patch intensities and positions to the voxel combined with the mean atlas CT value. A study examined atlas based techniques for brain compared single atlas, multi-atlas and multi-atlas followed by pattern recognition using gaussian process regression. They found that multi-atlas performed better than single however the gaussian regression did not improve over the use of a mean CT value from the atlas(Uh *et al.*, 2014). More recently a patch-based method has also been applied, where cubic patches of MRI images are compared to patches in an atlas database of co-registered MRI/CT scan pairs following affine registration. The most similar patches from a local neighborhood search of the atlas scans are used to produce the HU value(Andreasen *et al.*, 2016). For generation of prostate synthetic CT a multi-atlas registration to the acquired MRI from a large MRI/CT database has been employed. This was followed by voxel based weighting of atlas HU values according to the acquired voxel MRI similarities to the registered atlas voxels(Dowling *et al.*, 2015). The applicability of this method to 1.5T has recently been demonstrated(Wyatt *et al.*, 2017). A similar approach termed ‘statistical decomposition algorithm’ uses atlas scans that are deformably registered to the acquired MRI with a first registration used to drive segmentation of tissue classes on the acquired MRI and then a second structure-guided registration using the segmentations. HU values are then assigned by weighting the atlas HU values according to MRI similarities to the corresponding MRI atlas voxels(Siversson *et al.*, 2015). A multi-atlas method for head and neck synthetic CT has been developed that registers the atlas MRI scans (12 patients) to the target MRI and uses a generalized registration error (GRE) metric. The final synthetic CT value at each point is a nonlinear GRE-weighted average of the atlas CTs (Farjam *et al.*, 2017). A method that combines

regression based assignment of HU to soft tissue classes and atlas based bone HU assignment has been developed. The bone in the target MRI scan is segmented and the most similar bone in the atlas is deformably registered to the MRI and combined with the tissue-specific HU maps to generate the synthetic CT (Ghose *et al.*, 2017b). Recently a method for brain used a probability density function to estimate HU from the MRI signal value for the acquired voxel in T1 and T2 weighted images along with the voxel location in a reference anatomy derived from deformable registration to an atlas scan(Ren *et al.*, 2017). Synthetic CT for cervix and lung have also been developed by a combination of atlas based bone registration and soft-tissue classification.(Ren *et al.*, 2017; Andreasen *et al.*, 2016; Dowling *et al.*, 2012; Dowling *et al.*, 2015; Edmund *et al.*, 2014; Rivest-Hénault *et al.*, 2015; Kim *et al.*, 2015c; Zheng *et al.*, 2015; Wang *et al.*, 2017; Liu *et al.*, 2017a).

To date, two clinically released MR-only packages are clinically available for prostate cancer. One solution, Philips MR-CAT, is FDA-approved and integrated inline with the MRI reconstruction software to generate synthetic CT images immediately after the acquired MRI images have been reconstructed. This software employs a dual echo 3D mDIXON fast field echo sequence to generate synthetic CT using assigned bulk HU values for air, adipose, water, trabecular/spongy bone and compact/cortical bone(Tyagi *et al.*, 2016). Another commercially available product, Spectronic's MriPlanner, is regulatory approved (CE-marked) and requires end-users to upload a T2-weighted dataset for generation of synthetic CT. A statistical decomposition algorithm (SDA) is used as described above(Siversson *et al.*, 2015). Examples of preclinical and clinical implementations of synthetic CT for brain, prostate and female pelvis are provided below.

MRI-only planning: brain

One of the challenges with MRI-only planning of the brain is the presence of small, intricate air cavities and thin bones. Because bone has very short T2*, UTE pulse sequences may be employed to improve contrast between bone and surrounding air or soft tissue(Johansson *et al.*, 2011b; Robson *et al.*, 2003). One such solution has been implemented at Henry Ford Health System, where a combined UTE-mDixon sequence (TE1/TE2/TE3 = 0.144/3.4/6.9ms) was implemented on a 1.0T MR simulator(Zheng *et al.*, 2015). A hybrid MRI phase/magnitude UTE image processing pipeline was developed consisting of two major workflows: (1) generation of a bone-enhanced image that significantly improved bone and air contrast in MRI and (2) segmenting air regions of interest from UTE phase data combined with Gaussian mixture modeling (GMM). A previously developed synthetic CT pipeline for the pelvis was modified by incorporating derived bone-enhanced images and air masks into the workflow with bone-enhanced, FLAIR, and UTE images. Images were semi-automatically segmented into five categories (air, bone, fat, brain matter, and CSF) using a 5-kernel GMM before generating synthetic CTs using a region-specific, voxel-based weighted summation method described previously. Overall, results agree well with clinical CTs for treatment planning with mean absolute errors (MAE) between synthetic CT and CT-SIM of 147.5±8.3 HU which was consistent with literature. The MAE in the brain tends to be higher than that in the pelvis because of challenging segmentation yielding larger errors near bone-air interfaces. A voxel-based comparison in the brain by Johansson et. al yielded an average MAE of 137 HU (Johansson *et al.*, 2011a). Similarly, atlas-based methods

implemented in the brain have reported a wide range of MAE values, with differences of up to 600 HU found in bone (Demol *et al.*, 2016). Typical synthetic CT results are shown in Figure 5 for a post-surgical subject and a corresponding radiosurgery plan (18 Gy, 1 fraction, 8.8 cc planning target volume) calculated in Eclipse TPS using the anisotropic analytical algorithm (Varian, Palo Alto, CA) on both reference datasets, illustrating excellent dosimetric agreement between plans (negligible difference in target volume coverage) despite the lesion being situated near the bone and sinuses.

For an atlas-based approach, DVH differences between an atlas-based synCT and CT were ~3% except for cases where the tumors were located within the sphenoid bone and dose differences were observed up to 5–7% (Demol *et al.*, 2016). Recent work by Paradis et al. evaluated VMAT treatment plans in a 12 patient cohort and found no significant differences between calculated doses and planning constraints (OARs had an average D(max) differences of 0.0 Gy (−2.2 to 1.9 Gy)(Paradis *et al.*, 2015).

MRI-only planning: prostate

A site that has received considerable attention for MRI-only workflows due to the large patient numbers is prostate. Figure 6 shows an example of a synthetic CT generated for prostate using a voxel based calibration method(Korhonen *et al.*, 2014). This method has been implemented clinically at Helsinki University Central Hospital with nearly 400 prostate cancer patients treated with the MRI-only workflow since 2012. Bones are auto-segmented using at atlas based algorithm and separate mappings of MRI signal intensity to HU number performed for within bone and outside bone voxels. Recently the method has been generalized to other institutions and scanner types with similar results(Koivula *et al.*, 2017).

MRI-only planning: female pelvis

The development of synthetic CT for female pelvis has been more limited than for male, although preliminary results are emerging, often consisting of incorporating a bone shape model built from CT data (Liu *et al.*, 2017b; Liu *et al.*, 2015). Volumetric modulated arc therapy (VMAT) plans between synthetic CT and CT were found to have similar dosimetric agreement. Recent work has been performed translating male pelvis solutions to female anatomy for a voxel-based weighted summation technique(Kim *et al.*, 2017). Overall, synthetic CT weighting produced small changes for MAE and calculated dose distributions, suggesting that male pelvis weights are good approximations of female data. However, 3D treatment plans were found to be slightly more sensitive than VMAT patients, likely due to the attenuation through the femoral bones and need for more robust bone solutions.

Dose calculation accuracy in synthetic CT images

Methods of generating synthetic images need to be evaluated for HU accuracy and by comparing the calculated dose distribution in the generated synthetic CT image set and corresponding registered CT image set. Dose calculation around tissue boundaries where there is electron density alteration can be challenging and therefore, accurate representation of tissue inhomogeneity in synthetic CT images is important. It has been shown in previous studies that accurate representation of tissue inhomogeneity in synthetic CT images can improve dose calculation accuracy(Chen *et al.*, 2004a; Dowling *et al.*, 2012; Eilertsen *et al.*,

2008; Greer *et al.*, 2011; Johansson *et al.*, 2013; Johansson *et al.*, 2011b; Johansson *et al.*, 2012; Jonsson *et al.*, 2010; Kapanen and Tenhunen, 2013; Karotki *et al.*, 2011; Lambert *et al.*, 2011b; Lee *et al.*, 2003; Nyholm and Jonsson, 2014; Pasquier *et al.*, 2006; Stanescu *et al.*, 2006; Yu *et al.*, 2014). For example, treatment plans generated for prostate cancer patients show some differences in calculated dose performed in synthetic CT images compared to standard CT images. It has been shown that the dose difference for synthetic CT images assuming the whole body as water equivalent is within 4% and for synthetic CT images using bulk density assignment and atlas-based electron density mapping, the dose differences were within 3% and 2%, respectively(Chen *et al.*, 2004a; Dowling *et al.*, 2012; Greer *et al.*, 2011; Jonsson *et al.*, 2010; Kapanen and Tenhunen, 2013; Lambert *et al.*, 2011b; Lee *et al.*, 2003; Pasquier *et al.*, 2006). More sophisticated voxel and hybrid methods can yield dose differences to CT calculations typically less than 1% (Dowling *et al.*, 2012; Korhonen *et al.*, 2014). Some evaluations of the accuracy of the commercial methods have been recently reported(Tyagi *et al.*, 2016; Christiansen *et al.*, 2017; Persson *et al.*, 2017) showing dose differences generally within 1%. Overall, the dose calculation differences are larger for organ-at-risks (OARs) compared to targets.

Bone is an OAR where the synthetic CT representation is important and at same time challenging. Accurate representation of boundaries is important for bones since their misrepresentation will results in some dose calculation inaccuracies. However, delineating the bone boundaries is also challenging mainly because bony tissues pose a significant susceptibility artifact and this may cause boundary perturbation and shift. The effect of bony tissues boundary distortion on dose calculation accuracy especially for surrounding tissues has not been studied yet and more related studies are necessary as MRI-only treatment planning workflow is become more prevalent in routine clinical practice.

Position verification with MRI images

Position verification using MRI reference images presents some challenges due to the need for multi-modality image registration. One solution is to use MR sequences that can identify implanted fiducial markers. One such example is using a 3D balanced-FFE sequence to elucidate implanted gold fiducial markers in the pelvis that can then be contoured for use in IGRT (Tyagi *et al.*, 2016; Ghose *et al.*, 2016; Maspero *et al.*, 2017). In comparisons of 3D matching (i.e. CBCT to MR-CAT or standard CT-SIM) for 5 SBRT prostate cases (5 fractions/patient), mean differences were less than 1 mm for left-right and anterior-posterior while the superior-inferior direction was <0.5 mm. A few cases showed registration differences of >2 mm, mostly due to rotations. For 2D matching in 20 patients (planar KV images matched to MR-CAT bony anatomy and fiducials found on MRI), mean differences were <0.6 mm along each axis. In another study of 20 prostate cancer cases with 400 CBCTs evaluated with MRI as the reference dataset and daily shifts compared against CBCT-to-CT registration, shift positions for the cohort between CBCT-to-CT registration and CBCT-to-MRI registration are -0.15 ± 0.25 cm (anterior-posterior), 0.05 ± 0.19 cm (superior-inferior), and -0.01 ± 0.14 cm (left-right)(Doemer *et al.*, 2015b).

Other previous studies have demonstrated the possibility of position verification between MRI images that have been used for treatment planning and orthogonal 2D verification

images that have been acquired prior to treatment(Chen *et al.*, 2007; Chen *et al.*, 2004a; Kapanen and Tenhunen, 2013; Ramsey and Oliver, 1998; Yu *et al.*, 2014). Position verification using 2D images can be achieved by generating digitally reconstructed radiograph (synthetic-DRRs) from synthetic-CT (shown in Figure 7) and register them to the orthogonal projection images acquired prior to treatment. In a whole-brain IGRT study conducted by Yang *et al.* using orthogonal kV pairs in 7 patients found that all registrations were within 1 mm and 1 degree when aligned to their synthetic CT DRRs (Yang *et al.*, 2016). Yu *et al.* calculated differences between bony landmarks in MR-DRRs (derived from manually contoured T1-weighted datasets with CT number mapping) and CT-DRRs and found good general agreement although cases with differences of up to 1.9 mm in landmarks were observed(Yu *et al.*, 2014). In recent work by Price et al. studying registrations for 34-37 patient fractions, planar registrations had a mean shift differences were 0.4 ± 0.5 mm (range, −0.6 to 1.6 mm), 0.0 ± 0.5 mm (range, −0.9 to 1.2 mm), and 0.1 ± 0.3 mm (range, −0.7 to 0.6 mm) for the superior-inferior (S-I), left-right (L-R), and anterior-posterior (A-P) axes, respectively. For CBCT registrations, the mean shift differences in volumetric registrations were 0.6 ± 0.4 mm (range, −0.2 to 1.6 mm), 0.2 ± 0.4 mm (range, −0.3 to 1.2 mm), and 0.2 ± 0.3 mm (range, −0.2 to 1.2 mm) for the S-I, L-R, and A-P axes, respectively. The CT-SIM and synthetic CT derived margins were <0.3 mm different(Price *et al.*, 2016). Challenges have been realized in post-surgical areas, where resection cavities are not well characterized by synthetic CT solutions, which remains an area of potential opportunity.

Advanced Applications and Future Directions

MRI has the capabilities of providing comprehensive anatomical and functional information regarding the tumour and its surrounding normal structure with respect to tumour burden and response assessment. For example, MRI spectroscopy(Arias-Mendoza *et al.*, 2013; Glunde *et al.*, 2011; Harry *et al.*, 2010; Pinker *et al.*, 2012), diffusion-weighted imaging (DWI) (Padhani *et al.*, 2009; Tsien *et al.*, 2014), dynamic contrast-enhanced (DCE) perfusion imaging(Harry *et al.*, 2010),, and MRI elastography(Pepin *et al.*, 2014) are among the techniques that can be used to acquire functional information regarding tumour treatment response. Recently, a dose painting treatment planning pipeline was developed that incorporates functional multi-parametric MRI (including DWI and DCE) into an MR-only treatment planning workflow in the prostate with acceptable plan quality and excellent reproducibility(van Schie *et al.*, 2017).

Another challenge for synthetic CT includes MR-only planning for treatment sites that require motion management. Recent work evaluated MR-only planning for liver SBRT using a synthetic CT derived from a 3D gradient dual-echo Dixon sequence acquired at end-exhale (Bredfeldt *et al.*, 2017). Overall, excellent agreement was found between dose calculations on conventional CT-SIM data and synthetic CT, yielding <0.5 Gy difference for all metrics studied. A natural extension of this early work would be to incorporate four-dimensional MRI (4D-MRI) synthetic CT. 4D-MRI is becoming increasingly available in clinical and research prototypes including T2-weighted prospective acquisitions using external surrogates (Glide-Hurst *et al.*, 2015a; Du *et al.*, 2015), T1 and T2-weighted prospective acquisitions using internal navigators placed at the diaphragm/lung interface, and offline sorting using self-gating signal obtained from the k-space center (Freedman *et al.*, 2017) or

body area for a respiratory surrogate (Liu *et al.*, 2014). As 4D-MRI becomes more commercially available, it is expected that MR-only planning will undergo further development.

Conclusion

The accessibility to functional imaging and more accurate structural information leads to improved tumor delineation in MRI images compared with CT. As MRI scanners become more widely available with radiation therapy platforms, their use in radiation oncology clinical practice is slowly increasing. A wide range of approaches for generating synthetic CT images exist which seem to provide promising results applicable for clinical use. Most of these methods are based on currently available standard clinical MRI sequences. As the field transitions toward MRI-only treatment planning, CT images will not be required and all imaging data required for delineation and dose calculation will be provided by MRI. To fully implement MR-only workflows in radiation therapy, patients must be set up in their treatment positions in the MRI simulator with appropriate immobilization devices.

Acknowledgments

Research reported in this publication was supported by the National Cancer Institute of the National Institutes of Health under Award Number R01CA204189. The content is solely the responsibility of the authors and does not necessarily represent the official views of the National Institutes of Health. Carri Glide-Hurst reports research agreements with Philips Healthcare, Modus Medical Devices, and ViewRay, Inc.

References

Andreasen D, Van Leemput K, Edmund JM. A patch-based pseudo-CT approach for MRI-only radiotherapy in the pelvis. Med Phys. 2016; 43:4742. [PubMed: 27487892]

Arias-Mendoza F, Payne GS, Zakian K, Stubbs M, O'Connor OA, Mojahed H, Smith MR, Schwarz AJ, Shukla-Dave A, Howe F, Poptani H, Lee S-C, Pettengel R, Schuster SJ, Cunningham D, Heerschap A, Glickson JD, Griffiths JR, Koutcher JA, Leach MO, Brown TR. Noninvasive phosphorus magnetic resonance spectroscopic imaging predicts outcome to first-line chemotherapy in newly diagnosed patients with diffuse large B-cell lymphoma. Academic radiology. 2013; 20:1122–9. [PubMed: 23931426]

Baldwin LN, Wachowicz K, Thomas SD, Rivest R, Fallone BG. Characterization, prediction, and correction of geometric distortion in 3 T MR images. Med Phys. 2007a; 34:388. [PubMed: 17388155]

Baldwin LN, Wachowicz K, Thomas SD, Rivest R, Fallone BG. Characterization, prediction, and correction of geometric distortion in 3 T MR images. Medical physics. 2007b; 34:388–99. [PubMed: 17388155]

Baldwin LN, Wachowicz K, Thomas SD, Rivest R, Fallone BG. Characterization, prediction, and correction of geometric distortion in 3 T MR images. Medical physics. 2007c; 34:388–99. [PubMed: 17388155]

Beavis AW, Gibbs P, Dealey RA, Whitton VJ. Radiotherapy treatment planning of brain tumours using MRI alone. The British journal of radiology. 1998; 71:544–8. [PubMed: 9691900]

Bredfeldt JS, Liu L, Feng M, Cao Y, Balter JM. Synthetic CT for MRI-based liver stereotactic body radiotherapy treatment planning. Physics in medicine and biology. 2017; 62:2922. [PubMed: 28306547]

Burgos N, Cardoso MJ, Modat M, Pedemonte S, Dickson J, Barnes A, Duncan JS, Atkinson D, Arridge SR, Hutton BF, Ourselin S, Atkinson D, Arridge SR, Hutton BF, Ourselin S. Attenuation correction synthesis for hybrid PET-MR scanners. Medical image computing and computer-assisted

intervention: MICCAI … International Conference on Medical Image Computing and Computer-Assisted Intervention. 2013; 16:147–54.

Butts K, Pauly JM, Gold GE. Reduction of blurring in view angle tilting MRI. Magnetic resonance in medicine. 2005; 53:418–24. [PubMed: 15678535]

Caramanos Z, Fonov VS, Francis SJ, Narayanan S, Pike GB, Collins DL, Arnold DL. Gradient distortions in MRI: characterizing and correcting for their effects on SIENA-generated measures of brain volume change. NeuroImage. 2010; 49:1601–11. [PubMed: 19682586]

Catana C, van der Kouwe A, Benner T, Michel CJ, Hamm M, Fenchel M, Fischl B, Rosen B, Schmand M, Sorensen AG. Toward implementing an MRI-based PET attenuation-correction method for neurologic studies on the MR-PET brain prototype. J Nucl Med. 2010; 51:1431–8. [PubMed: 20810759]

Chang EL, Akyurek S, Avalos T, Rebueno N, Spicer C, Garcia J, Famiglietti R, Allen PK, Chao KC, Mahajan A. Evaluation of peritumoral edema in the delineation of radiotherapy clinical target volumes for glioblastoma. International Journal of Radiation Oncology* Biology* Physics. 2007; 68:144–50.

Chen AM, Farwell DG, Luu Q, Chen LM, Vijayakumar S, Purdy JA. Marginal Misses After Postoperative Intensity-Modulated Radiotherapy for Head and Neck Cancer. International Journal of Radiation Oncology*Biology*Physics. 2011; 80:1423–9.

Chen L, Nguyen T-B, Jones É, Chen Z, Luo W, Wang L, Price RA, Pollack A, Ma C-MC. Magnetic Resonance–Based Treatment Planning for Prostate Intensity-Modulated Radiotherapy: Creation of Digitally Reconstructed Radiographs. International Journal of Radiation Oncology*Biology*Physics. 2007; 68:903–11.

Chen L, Price RA, Nguyen T-B, Wang L, Li JS, Qin L, Ding M, Palacio E, Ma C-M, Pollack A. Dosimetric evaluation of MRI-based treatment planning for prostate cancer. Physics in medicine and biology. 2004a; 49:5157–70. [PubMed: 15609565]

Chen L, Price RA, Wang L, Li J, Qin L, McNeeley S, Ma C-MC, Freedman GM, Pollack A. MRI-based treatment planning for radiotherapy: Dosimetric verification for prostate IMRT. International Journal of Radiation Oncology*Biology*Physics. 2004b; 60:636–47.

Chen ME, Troncoso P, Johnston DA, Tang K, Babaian JR. Optimization of prostate biopsy strategy using computer based analysis. The Journal of urology. 1997; 158:2168–75. [PubMed: 9366337]

Choi S-J, Koch KM, Hargreaves BA, Stevens KJ, Gold GE. Metal artifact reduction with MAVRIC SL at 3-T MRI in patients with hip arthroplasty. AJR American journal of roentgenology. 2015; 204:140–7. [PubMed: 25539249]

Christiansen RL, Jensen HR, Brink C. Magnetic resonance only workflow and validation of dose calculations for radiotherapy of prostate cancer. Acta Oncol. 2017; 56:787–91. [PubMed: 28464739]

Debois M, Oyen R, Maes F, Verswijvel G, Gatti G, Bosmans H, Feron M, Bellon E, Kutcher G, Van Poppel H, Vanuytsel L. The contribution of magnetic resonance imaging to the three-dimensional treatment planning of localized prostate cancer. International Journal of Radiation Oncology*Biology*Physics. 1999; 45:857–65.

Demol B, Boydev C, Korhonen J, Reynaert N. Dosimetric characterization of MRI-only treatment planning for brain tumors in atlas-based pseudo-CT images generated from standard T1-weighted MR images. Medical physics. 2016; 43:6557–68. [PubMed: 27908187]

Devic S. MRI simulation for radiotherapy treatment planning. Med Phys. 2012; 39:6701. [PubMed: 23127064]

Doemer A, Chetty IJ, Glide-Hurst C, Nurushev T, Hearshen D, Pantelic M, Traughber M, Kim J, Levin K, Elshaikh MA. Evaluating organ delineation, dose calculation and daily localization in an open-MRI simulation workflow for prostate cancer patients. Radiation Oncology. 2015a; 10:37. [PubMed: 25889107]

Doemer A, Chetty IJ, Glide-Hurst C, Nurushev T, Hearshen D, Pantelic M, Traughber M, Kim J, Levin K, Elshaikh MA, Walker E, Movsas B. Evaluating organ delineation, dose calculation and daily localization in an open-MRI simulation workflow for prostate cancer patients. Radiation oncology (London, England). 2015b; 10:37.

Doran SJ, Charles-Edwards L, Reinsberg SA, Leach MO. A complete distortion correction for MR images: I. Gradient warp correction. Physics in medicine and biology. 2005; 50:1343–61. [PubMed: 15798328]

Dowling JA, Lambert J, Parker J, Salvado O, Fripp J, Capp A, Wratten C, Denham JW, Greer PB. An Atlas-Based Electron Density Mapping Method for Magnetic Resonance Imaging (MRI)-Alone Treatment Planning and Adaptive MRI-Based Prostate Radiation Therapy. International Journal of Radiation Oncology*Biology*Physics. 2012; 83:e5–e11.

Dowling JA, Sun J, Pichler P, Rivest-Hénault D, Ghose S, Richardson H, Wratten C, Martin J, Arm J, Best L, Chandra SS, Fripp J, Menk FW, Greer PB. Automatic Substitute Computed Tomography Generation and Contouring for Magnetic Resonance Imaging (MRI)-Alone External Beam Radiation Therapy From Standard MRI Sequences. International journal of radiation oncology, biology, physics. 2015; 93:1144–53.

Du D, Caruthers SD, Glide-Hurst C, Low DA, Li HH, Mutic S, Hu Y. High-quality T2-weighted 4-dimensional magnetic resonance imaging for radiation therapy applications. International Journal of Radiation Oncology* Biology* Physics. 2015; 92:430–7.

Edmund JM, Kjer HM, Van Leemput K, Hansen RH, Andersen JAL, Andreasen D. A voxel-based investigation for MRI-only radiotherapy of the brain using ultra short echo times. Physics in medicine and biology. 2014; 59:7501–19. [PubMed: 25393873]

Edmund JM, Nyholm T. A review of substitute CT generation for MRI-only radiation therapy. Radiation oncology (London, England). 2017; 12:28.

Eilertsen K, Vestad LNTA, Geier O, Skretting A. A simulation of MRI based dose calculations on the basis of radiotherapy planning CT images. Acta oncologica (Stockholm, Sweden). 2008; 47:1294–302.

Farjam R, Tyagi N, Veeraraghavan H, Apte A, Zakian K, Hunt MA, Deasy JO. Multiatlas approach with local registration goodness weighting for MRI-based electron density mapping of head and neck anatomy. Medical Physics. 2017; 44:3706–17. [PubMed: 28444772]

Freedman JN, Collins DJ, Bainbridge H, Rank CM, Nill S, Kachelrieß M, Oelfke U, Leach MO, Wetscherek A. T2-Weighted 4D Magnetic Resonance Imaging for Application in Magnetic Resonance-Guided Radiotherapy Treatment Planning. 2017

Garcia-Alvarez R, Liney GP, Beavis AW. Repeatability of functional MRI for conformal avoidance radiotherapy planning. J Magn Reson Imaging. 2006; 23:108–14. [PubMed: 16416436]

Gay HA, Barthold HJ, O'Meara E, Bosch WR, El Naqa I, Al-Lozi R, Rosenthal SA, Lawton C, Lee WR, Sandler H, Zietman A, Myerson R, Dawson LA, Willett C, Kachnic LA, Jhingran A, Portelance L, Ryu J, Small W Jr, Gaffney D, Viswanathan AN, Michalski JM. Pelvic Normal Tissue Contouring Guidelines for Radiation Therapy: ARadiation Therapy Oncology Group Consensus Panel Atlas. International Journal of Radiation Oncology*Biology*Physics. 2012; 83:e353–e62.

Ghose S, Dowling JA, Rai R, Liney GP. Substitute CT generation from a single ultra short time echo MRI sequence: Preliminary study. Physics in Medicine and Biology. 2017a; 62:2950–60. [PubMed: 28306546]

Ghose S, Greer PB, Sun J, Pichler P, Rivest-Henault D, Mitra J, Richardson H, Wratten C, Martin J, Arm J, Best L, Dowling JA. Regression and statistical shape model based substitute CT generation for MRI alone external beam radiation therapy from standard clinical MRI sequences. Phys Med Biol. 2017b; 62:8566–80. [PubMed: 28976369]

Ghose S, Mitra J, Rivest-Henault D, Fazlollahi A, Stanwell P, Pichler P, Sun J, Fripp J, Greer PB, Dowling JA. MRI-alone radiation therapy planning for prostate cancer: Automatic fiducial marker detection. Med Phys. 2016; 43:2218. [PubMed: 27147334]

Giezen M, Kouwenhoven E, Scholten AN, Coerkamp EG, Heijenbrok M, Jansen WP, Mast ME, Petoukhova AL, Struikmans H. MRI- versus CT-based volume delineation of lumpectomy cavity in supine position in breast-conserving therapy: an exploratory study. Int J Radiat Oncol Biol Phys. 2012; 82:1332–40. [PubMed: 21708426]

Glide-Hurst CK, Kim JP, To D, Hu Y, Kadbi M, Nielsen T, Chetty IJ. Four dimensional magnetic resonance imaging optimization and implementation for magnetic resonance imaging simulation. Practical radiation oncology. 2015a; 5:433–42. [PubMed: 26419444]

Glide-Hurst CK, Wen N, Hearshen D, Kim J, Pantelic M, Zhao B, Mancell T, Levin K, Movsas B, Chetty IJ. Initial clinical experience with a radiation oncology dedicated open 1.0 T MR-simulation. Journal of Applied Clinical Medical Physics. 2015b; 16

Glunde K, Bhujwalla ZM, Ronen SM. Choline metabolism in malignant transformation. Nature reviews Cancer. 2011; 11:835–48. [PubMed: 22089420]

Greer PB, Dowling JA, Lambert JA, Fripp J, Parker J, Denham JW, Wratten C, Capp A, Salvado O. A magnetic resonance imaging-based workflow for planning radiation therapy for prostate cancer. The Medical journal of Australia. 2011; 194:S24–7. [PubMed: 21401484]

Haider MA, Chung P, Sweet J, Toi A, Jhaveri K, Menard C, Warde P, Trachtenberg J, Lockwood G, Milosevic M. Dynamic contrast-enhanced magnetic resonance imaging for localization of recurrent prostate cancer after external beam radiotherapy. Int J Radiat Oncol. 2008; 70:425–30.

Hamstra DA, Galban CJ, Meyer CR, Johnson TD, Sundgren PC, Tsien C, Lawrence TS, Junck L, Ross DJ, Rehemtulla A, Ross BD, Chenevert TL. Functional diffusion map as an early imaging biomarker for high-grade glioma: Correlation with conventional radiologic response and overall survival. J Clin Oncol. 2008; 26:3387–94. [PubMed: 18541899]

Han X. MR-based synthetic CT generation using a deep convolutional neural network method. Med Phys. 2017; 44:1408–19. [PubMed: 28192624]

Hargreaves BA, Worters PW, Pauly KB, Pauly JM, Koch KM, Gold GE. Metal-induced artifacts in MRI. AJR American journal of roentgenology. 2011; 197:547–55. [PubMed: 21862795]

Harry VN, Semple SI, Parkin DE, Gilbert FJ. Use of new imaging techniques to predict tumour response to therapy. The Lancet Oncology. 2010; 11:92–102. [PubMed: 20129132]

Hellebust TP, Kirisits C, Berger D, Pérez-Calatayud J, De Brabandere M, De Leeuw A, Dumas I, Hudej R, Lowe G, Wills R, Tanderup K, Group G G G-E W. Recommendations from Gynaecological (GYN) GEC-ESTRO Working Group: considerations and pitfalls in commissioning and applicator reconstruction in 3D image-based treatment planning of cervix cancer brachytherapy. Radiotherapy and oncology: journal of the European Society for Therapeutic Radiology and Oncology. 2010; 96:153–60. [PubMed: 20663578]

Hentschel B, Oehler W, Strauss D, Ulrich A, Malich A. Definition of the CTV prostate in CT and MRI by using CT-MRI image fusion in IMRT planning for prostate cancer. Strahlentherapie und Onkologie: Organ der Deutschen Rontgengesellschaft … [et al]. 2011; 187:183–90.

Hofmann M, Steinke F, Scheel V, Charpiat G, Farquhar J, Aschoff P, Brady M, Scholkopf B, Pichler BJ. MRI-based attenuation correction for PET/MRI: a novel approach combining pattern recognition and atlas registration. J Nucl Med. 2008; 49:1875–83. [PubMed: 18927326]

Hsu S-H, Cao Y, Huang K, Feng M, Balter JM. Investigation of a method for generating synthetic CT models from MRI scans of the head and neck for radiation therapy. Physics in medicine and biology. 2013a; 58:8419–35. [PubMed: 24217183]

Hsu S-H, Cao Y, Lawrence TS, Tsien C, Feng M, Grodzki DM, Balter JM. Quantitative characterizations of ultrashort echo (UTE) images for supporting air-bone separation in the head. Physics in medicine and biology. 2015a; 60:2869–80. [PubMed: 25776205]

Hsu S-H, Cao Y, Lawrence TS, Tsien C, Feng M, Grodzki DM, Balter JM. Quantitative characterizations of ultrashort echo (UTE) images for supporting air–bone separation in the head. Phys Med Biol. 2015b; 60:2869–80. [PubMed: 25776205]

Hsu SH, Cao Y, Huang K, Feng M, Balter JM. Investigation of a method for generating synthetic CT models from MRI scans of the head and neck for radiation therapy. Physics in medicine and biology. 2013b; 58:8419–35. [PubMed: 24217183]

Huang KC, Cao Y, Baharom U, Balter JM. Phantom-based characterization of distortion on a magnetic resonance imaging simulator for radiation oncology. Physics in medicine and biology. 2016a; 61:774. [PubMed: 26732744]

Huang KC, Cao Y, Baharom U, Balter JM. Phantom-based characterization of distortion on a magnetic resonance imaging simulator for radiation oncology. Physics in medicine and biology. 2016b; 61:774–90. [PubMed: 26732744]

Janke A, Zhao H, Cowin GJ, Galloway GJ, Doddrell DM. Use of spherical harmonic deconvolution methods to compensate for nonlinear gradient effects on MRI images. Magnetic resonance in medicine. 2004; 52:115–22. [PubMed: 15236374]

Johansson A, Garpebring A, Karlsson M, Asklund T, Nyholm T. Improved quality of computed tomography substitute derived from magnetic resonance (MR) data by incorporation of spatial information--potential application for MR-only radiotherapy and attenuation correction in positron emission tomography. Acta oncologica (Stockholm, Sweden). 2013; 52:1369–73.

Johansson A, Karlsson M, Nyholm T. CT substitute derived from MRI sequences with ultrashort echo time. Med Phys. 2011a; 38:2708–14. [PubMed: 21776807]

Johansson A, Karlsson M, Nyholm T. CT substitute derived from MRI sequences with ultrashort echo time. Medical physics. 2011b; 38:2708–14. [PubMed: 21776807]

Johansson A, Karlsson M, Yu J, Asklund T, Nyholm T. Voxel-wise uncertainty in CT substitute derived from MRI. Medical physics. 2012; 39:3283–90. [PubMed: 22755711]

Johnstone E, Wyatt JJ, Henry AM, Short SC, Sebag-Montefiore D, Murray L, Kelly CG, McCallum HM, Speight R. A systematic review of synthetic CT generation methodologies for use in MRI-only radiotherapy. International Journal of Radiation Oncology*Biology*Physics. 2017

Jolicoeur M, Racine M-L, Trop I, Hathout L, Nguyen D, Derashodian T, David S. Localization of the surgical bed using supine magnetic resonance and computed tomography scan fusion for planification of breast interstitial brachytherapy. Radiotherapy and Oncology. 2011; 100:480–4. [PubMed: 21924509]

Jonsson JH, Karlsson MG, Karlsson M, Nyholm T. Treatment planning using MRI data: an analysis of the dose calculation accuracy for different treatment regions. Radiation oncology (London, England). 2010; 5:62.

Jovicich J, Czanner S, Greve D, Haley E, van der Kouwe A, Gollub R, Kennedy D, Schmitt F, Brown G, Macfall J, Fischl B, Dale A. Reliability in multi-site structural MRI studies: effects of gradient non-linearity correction on phantom and human data. NeuroImage. 2006; 30:436–43. [PubMed: 16300968]

Just M, Rösler HP, Higer HP, Kutzner J, Thelen M. MRI-assisted radiation therapy planning of brain tumors-clinical experiences in 17 patients. Magnetic Resonance Imaging. 1991; 9:173–7. [PubMed: 2034050]

Kapanen M, Collan J, Beule A, Seppala T, Saarilahti K, Tenhunen M. Commissioning of MRI-only based treatment planning procedure for external beam radiotherapy of prostate. Magnetic resonance in medicine: official journal of the Society of Magnetic Resonance in Medicine/Society of Magnetic Resonance in Medicine. 2012

Kapanen M, Collan J, Beule A, Seppala T, Saarilahti K, Tenhunen M. Commissioning of MRI-only based treatment planning procedure for external beam radiotherapy of prostate. Magnetic resonance in medicine: official journal of the Society of Magnetic Resonance in Medicine/Society of Magnetic Resonance in Medicine. 2013; 70:127–35.

Kapanen M, Tenhunen M. T1/T2*-weighted MRI provides clinically relevant pseudo-CT density data for the pelvic bones in MRI-only based radiotherapy treatment planning. Acta oncologica (Stockholm, Sweden). 2013; 52:612–8.

Karlsson M, Karlsson MG, Nyholm T, Amies C, Zackrisson B. Dedicated magnetic resonance imaging in the radiotherapy clinic. International journal of radiation oncology, biology, physics. 2009; 74:644–51.

Karotki A, Mah K, Meijer G, Meltsner M. Comparison of bulk electron density and voxel-based electron density treatment planning. Journal of applied clinical medical physics. 2011; 12:3522. [PubMed: 22089006]

Keereman V, Fierens Y, Broux T, De Deene Y, Lonneux M, Vandenberghe S. MRI-based attenuation correction for PET/MRI using ultrashort echo time sequences. J Nucl Med. 2010; 51:812–8. [PubMed: 20439508]

Khoo VS, Joon DL. New developments in MRI for target volume delineation in radiotherapy. The British journal of radiology. 2006:S2–15. [PubMed: 16980682]

Kim J, Garbarino K, Schultz L, Levin K, Movsas B, Siddiqui MS, Chetty IJ, Glide-Hurst C. Dosimetric evaluation of synthetic CT relative to bulk density assignment-based magnetic resonance-only approaches for prostate radiotherapy. Radiation Oncology. 2015a; 10:239. [PubMed: 26597251]

Kim J, Garbarino K, Schultz L, Levin K, Movsas B, Siddiqui MS, Chetty IJ, Glide-Hurst C. Dosimetric evaluation of synthetic CT relative to bulk density assignment-based magnetic resonance-only approaches for prostate radiotherapy. Radiation Oncology. 2015b; 10:1. [PubMed: 25567003]

Kim J, Ghanem A, Elshaikh M, Chetty I, Glide-Hurst C. MO-RAM-GePD-JT-2 Optimization of Synthetic CT for Female Pelvis. Med Phys. 2017

Kim J, Glide-Hurst C, Doemer A, Wen N, Movsas B, Chetty IJ. Implementation of a Novel Algorithm For Generating Synthetic CT Images From Magnetic Resonance Imaging Data Sets for Prostate Cancer Radiation Therapy. International Journal of Radiation Oncology* Biology* Physics. 2015c; 91:39–47.

Kim RY, McGinnis LS, Spencer SA, Meredith RF, Jennelle RL, Salter MM. Conventional four-field pelvic radiotherapy technique without computed tomography-treatment planning in cancer of the cervix: potential geographic miss and its impact on pelvic control. International Journal of Radiation Oncology* Biology* Physics. 1995; 31:109–12.

Kirisits C, Rivard MJ, Baltas D, Ballester F, De Brabandere M, van der Laarse R, Niatsetski Y, Papagiannis P, Hellebust TP, Perez-Calatayud J, Tanderup K, Venselaar JLM, Siebert F-A. Review of clinical brachytherapy uncertainties: analysis guidelines of GEC-ESTRO and the AAPM. Radiotherapy and oncology: journal of the European Society for Therapeutic Radiology and Oncology. 2014; 110:199–212. [PubMed: 24299968]

Koch KM, Brau AC, Chen W, Gold GE, Hargreaves BA, Koff M, McKinnon GC, Potter HG, King KF. Imaging near metal with a MAVRIC-SEMAC hybrid. Magnetic resonance in medicine. 2011; 65:71–82. [PubMed: 20981709]

Koch KM, Lorbiecki JE, Hinks RS, King KF. A multispectral three-dimensional acquisition technique for imaging near metal implants. Magnetic resonance in medicine. 2009; 61:381–90. [PubMed: 19165901]

Koivula L, Kapanen M, Seppälä T, Collan J, Dowling JA, Greer PB, Gustafsson C, Gunnlaugsson A, Olsson LE, Wee L, Korhonen J. Intensity-based dual model method for generation of synthetic CT images from standard T2-weighted MR images – Generalized technique for four different MR scanners. Radiotherapy and Oncology. 2017

Korhonen J, Kapanen M, Keyrilainen J, Seppala T, Tenhunen M. A dual model HU conversion from MRI intensity values within and outside of bone segment for MRI-based radiotherapy treatment planning of prostate cancer. Medical Physics. 2014; 41

Korsholm ME, Waring LW, Edmund JM. A criterion for the reliable use of MRI-only radiotherapy. Radiation oncology (London, England). 2014; 9:16.

Kovacs A, Toth L, Glavak C, Liposits G, Hadjiev J, Antal G, Emri M, Vandulek C, Repa I. Integrating functional MRI information into conventional 3D radiotherapy planning of CNS tumors. Is it worth it? J Neuro-Oncol. 2011; 105:629–37.

Lambert J, Greer PB, Menk F, Patterson J, Parker J, Dahl K, Gupta S, Capp A, Wratten C, Tang C, Kumar M, Dowling J, Hauville S, Hughes C, Fisher K, Lau P, Denham JW, Salvado O. MRI-guided prostate radiation therapy planning: Investigation of dosimetric accuracy of MRI-based dose planning. Radiotherapy and Oncology. 2011a; 98:330–4. [PubMed: 21339009]

Lambert J, Greer PB, Menk F, Patterson J, Parker J, Dahl K, Gupta S, Capp A, Wratten C, Tang C, Kumar M, Dowling J, Hauville S, Hughes C, Fisher K, Lau P, Denham JW, Salvado O. MRI-guided prostate radiation therapy planning: Investigation of dosimetric accuracy of MRI-based dose planning. Radiotherapy and oncology: journal of the European Society for Therapeutic Radiology and Oncology. 2011b; 98:330–4. [PubMed: 21339009]

Lee GN, Fujita H. K-means Clustering for Classifying Unlabelled MRI Data. 9th Biennial Conference of the Australian Pattern Recognition Society on Digital Image Computing Techniques and Applications (DICTA 2007): IEEE). 2007:92–8.

Lee YK, Bollet M, Charles-Edwards G, Flower MA, Leach MO, McNair H, Moore E, Rowbottom C, Webb S. Radiotherapy treatment planning of prostate cancer using magnetic resonance imaging alone. Radiotherapy and oncology: journal of the European Society for Therapeutic Radiology and Oncology. 2003; 66:203–16. [PubMed: 12648793]

Levy A, Caramella C, Chargari C, Medjhoul A, Rey A, Zareski E, Boulet B, Bidault F, Dromain C, Balleyguier C. Accuracy of diffusion-weighted echo-planar MR imaging and ADC mapping in the

evaluation of residual cervical carcinoma after radiation therapy. Gynecol Oncol. 2011; 123:110–5. [PubMed: 21764110]

Liu L, Cao Y, Fessler JA, Jolly S, Balter JM. A female pelvic bone shape model for air/bone separation in support of synthetic CT generation for radiation therapy. Physics in medicine and biology. 2015; 61:169. [PubMed: 26624989]

Liu L, Jolly S, Cao Y, Vineberg K, Fessler JA, Balter JM. Female pelvic synthetic CT generation based on joint intensity and shape analysis. Phys Med Biol. 2017a; 62:2935–49. [PubMed: 28306550]

Liu L, Jolly S, Cao Y, Vineberg K, Fessler JA, Balter JM. Female pelvic synthetic CT generation based on joint intensity and shape analysis. Physics in medicine and biology. 2017b; 62:2935. [PubMed: 28306550]

Liu Y, Yin FF, Chang Z, Czito BG, Palta M, Bashir MR, Qin Y, Cai J. Investigation of sagittal image acquisition for 4D-MRI with body area as respiratory surrogate. Medical physics. 2014; 41

Lu W, Pauly KB, Gold GE, Pauly JM, Hargreaves BA. SEMAC: slice encoding for metal artifact correction in MRI. Magnetic Resonance in Medicine. 2009; 62:66–76. [PubMed: 19267347]

Lu W, Pauly KB, Gold GE, Pauly JM, Hargreaves BA. Slice encoding for metal artifact correction with noise reduction. Magnetic resonance in medicine. 2011; 65:1352–7. [PubMed: 21287596]

Maikusa N, Yamashita F, Tanaka K, Abe O, Kawaguchi A, Kabasawa H, Chiba S, Kasahara A, Kobayashi N, Yuasa T, Sato N, Matsuda H, Iwatsubo T, Initiative J A s D N. Improved volumetric measurement of brain structure with a distortion correction procedure using an ADNI phantom. Medical physics. 2013; 40:062303. [PubMed: 23718605]

Mardor Y, Pfeffer R, Spiegelmann R, Roth Y, Maier SE, Nissim O, Berger R, Glicksman A, Baram J, Orenstein A, Cohen JS, Tichler T. Early detection of response to radiation therapy in patients with brain malignancies using conventional and high b-value diffusion-weighted magnetic resonance imaging. J Clin Oncol. 2003; 21:1094–100. [PubMed: 12637476]

Martinez-Möller A, Nekolla SG. Attenuation correction for PET/MR: problems, novel approaches and practical solutions. Zeitschrift fur medizinische Physik. 2012; 22:299–310. [PubMed: 22925653]

Maspero M, van den Berg CAT, Zijlstra F, Sikkes GG, de Boer HCJ, Meijer GJ, Kerkmeijer LGW, Viergever MA, Lagendijk JJW, Seevinck PR. Evaluation of an automatic MR-based gold fiducial marker localisation method for MR-only prostate radiotherapy. Phys Med Biol. 2017; 62:7981–8002. [PubMed: 28825917]

McGee KP, Hu Y, Tryggestad E, Brinkmann D, Witte B, Welker K, Panda A, Haddock M, Bernstein MA. MRI in radiation oncology: Underserved needs. Magnetic Resonance in Medicine. 2015:n/a–n/a.

McGee KP, Hu Y, Tryggestad E, Brinkmann D, Witte B, Welker K, Panda A, Haddock M, Bernstein MA. MRI in radiation oncology: Underserved needs. Magnetic resonance in medicine. 2016; 75:11–4. [PubMed: 26173404]

McLaughlin PW, Narayana V, Meirovitz A, Troyer S, Roberson PL, Gonda R, Sandler H Jr, Marsh L, Lawrence T, Kessler M. Vessel-sparing prostate radiotherapy: dose limitation to critical erectile vascular structures (internal pudendal artery and corpus cavernosum) defined by MRI. Int J Radiat Oncol Biol Phys. 2005; 61:20–31. [PubMed: 15629590]

McVeigh PZ, Syed AM, Milosevic M, Fyles A, Haider MA. Diffusion-weighted MRI in cervical cancer. Eur Radiol. 2008; 18:1058–64. [PubMed: 18193428]

Nguyen PL, Aizer A, Assimos DG, D'Amico AV, Frank SJ, Gottschalk AR, Gustafson GS, Hsu IC, McLaughlin PW, Merrick G, Rosenthal SA, Showalter TN, Taira AV, Vapiwala N, Yamada Y, Davis BJ. ACR Appropriateness Criteria(R) Definitive External-Beam Irradiation in stage T1 and T2 prostate cancer. American journal of clinical oncology. 2014; 37:278–88. [PubMed: 25180754]

Njeh C. Tumor delineation: The weakest link in the search for accuracy in radiotherapy. Journal of medical physics/Association of Medical Physicists of India. 2008; 33:136.

Nyholm T, Jonsson J. Counterpoint: Opportunities and challenges of a magnetic resonance imaging-only radiotherapy work flow. Seminars in radiation oncology. 2014; 24:175–80. [PubMed: 24931088]

Padhani AR, Liu G, Koh DM, Chenevert TL, Thoeny HC, Takahara T, Dzik-Jurasz A, Ross BD, Van Cauteren M, Collins D, Hammoud DA, Rustin GJS, Taouli B, Choyke PL. Diffusion-weighted

magnetic resonance imaging as a cancer biomarker: consensus and recommendations. Neoplasia (New York, NY). 2009; 11:102–25.

Paradis E, Cao Y, Lawrence TS, Tsien C, Feng M, Vineberg K, Balter JM. Assessing the Dosimetric Accuracy of Magnetic Resonance-Generated Synthetic CT Images for Focal Brain VMAT Radiation Therapy. International Journal of Radiation Oncology*Biology*Physics. 2015; 93:1154–61.

Pasquier D, Betrouni N, Vermandel M, Lacornerie T, Lartigau E, Rousseau J. MRI alone simulation for conformal radiation therapy of prostate cancer: technical aspects. Conference proceedings: … Annual International Conference of the IEEE Engineering in Medicine and Biology Society IEEE Engineering in Medicine and Biology Society Annual Conference. 2006; 1:160–3.

Paulson ES, Erickson B, Schultz C, Allen Li X. Comprehensive MRI simulation methodology using a dedicated MRI scanner in radiation oncology for external beam radiation treatment planning. Med Phys. 2015; 42:28. [PubMed: 25563245]

Pepin KM, Chen J, Glaser KJ, Mariappan YK, Reuland B, Ziesmer S, Carter R, Ansell SM, Ehman RL, McGee KP. MR elastography derived shear stiffness-a new imaging biomarker for the assessment of early tumor response to chemotherapy. Magnetic Resonance in Medicine. 2014; 71:1834–40. [PubMed: 23801372]

Persson E, Gustafsson C, Nordstrom F, Sohlin M, Gunnlaugsson A, Petruson K, Rintela N, Hed K, Blomqvist L, Zackrisson B, Nyholm T, Olsson LE, Siversson C, Jonsson J. MR-OPERA: A Multicenter/Multivendor Validation of Magnetic Resonance Imaging-Only Prostate Treatment Planning Using Synthetic Computed Tomography Images. Int J Radiat Oncol Biol Phys. 2017

Pinker K, Stadlbauer A, Bogner W, Gruber S, Helbich TH. Molecular imaging of cancer: MR spectroscopy and beyond. European journal of radiology. 2012; 81:566–77. [PubMed: 20554145]

Pötter R, Dimopoulos J, Georg P, Lang S, Waldhäusl C, Wachter-Gerstner N, Weitmann H, Reinthaller A, Knocke TH, Wachter S, Kirisits C. Clinical impact of MRI assisted dose volume adaptation and dose escalation in brachytherapy of locally advanced cervix cancer. Radiotherapy and Oncology. 2007; 83:148–55. [PubMed: 17531904]

Pötter R, Haie-Meder C, Van Limbergen E, Barillot I, De Brabandere M, Dimopoulos J, Dumas I, Erickson B, Lang S, Nulens A. Recommendations from gynaecological (GYN) GEC ESTRO working group (II): concepts and terms in 3D image-based treatment planning in cervix cancer brachytherapy—3D dose volume parameters and aspects of 3D image-based anatomy, radiation physics, radiobiology. Radiotherapy and Oncology. 2006; 78:67–77. [PubMed: 16403584]

Price RG, Kadbi M, Kim J, Balter J, Chetty IJ, Glide-Hurst CK. Technical Note: Characterization and correction of gradient nonlinearity induced distortion on a 1.0 T open bore MR-SIM. Medical physics. 2015; 42:5955–60. [PubMed: 26429270]

Price RG, Kim JP, Zheng W, Chetty IJ, Glide-Hurst C. Image Guided Radiation Therapy Using Synthetic Computed Tomography Images in Brain Cancer. International Journal of Radiation Oncology*Biology*Physics. 2016; 95:1281–9.

Price RG, Knight RA, Hwang K, Bayram E, Nejad-Davarani SP, K.; G-H C. Optimization of a Novel Large Field of View Distortion Phantom for MR-Only Treatment Planning. Journal of Applied Clinical Medical Physics. 2017

Ramsey CR, Oliver AL. Magnetic resonance imaging based digitally reconstructed radiographs, virtual simulation, and three-dimensional treatment planning for brain neoplasms. Medical Physics. 1998; 25:1928. [PubMed: 9800700]

Rasch C, Barillot I, Remeijer P, Touw A, van Herk M, Lebesque JV. Definition of the prostate in CT and MRI: a multi-observer study. International journal of radiation oncology, biology, physics. 1999; 43:57–66.

Rasch C, Steenbakkers R, van Herk M. Target Definition in Prostate, Head, and Neck. Seminars in Radiation Oncology. 2005; 15:136–45. [PubMed: 15983939]

Reichert M, Ai T, Morelli JN, Nittka M, Attenberger U, Runge VM. Metal artefact reduction in MRI at both 1.5 and 3.0 T using slice encoding for metal artefact correction and view angle tilting. The British journal of radiology. 2015; 88:20140601. [PubMed: 25613398]

Ren S, Hara W, Wang L, Buyyounouski MK, Le QT, Xing L, Li R. Robust Estimation of Electron Density From Anatomic Magnetic Resonance Imaging of the Brain Using a Unifying Multi-Atlas Approach. Int J Radiat Oncol Biol Phys. 2017; 97:849–57. [PubMed: 28244422]

Rivest-Hénault D, Dowson N, Greer PB, Fripp J, Dowling JA. Robust inverse-consistent affine CT–MR registration in MRI-assisted and MRI-alone prostate radiation therapy. Medical image analysis. 2015; 23:56–69. [PubMed: 25966468]

Robson MD, Gatehouse PD, Bydder M, Bydder GM. Magnetic resonance: an introduction to ultrashort TE (UTE) imaging. Journal of computer assisted tomography. 2003; 27:825–46. [PubMed: 14600447]

Roy S, Butman JA, Pham DL. Synthesizing CT from ultrashort echo-time MR images via convolutional neural networks. Lecture Notes in Computer Science (including subseries Lecture Notes in Artificial Intelligence and Lecture Notes in Bioinformatics). 2017:24–32.

Schenck JF. The role of magnetic susceptibility in magnetic resonance imaging: MRI magnetic compatibility of the first and second kinds. Medical physics. 1996; 23:815–50. [PubMed: 8798169]

Schmidt MA, Payne GS. Radiotherapy planning using MRI. Physics in medicine and biology. 2015; 60:R323–61. [PubMed: 26509844]

Siversson C, Nordstrom F, Nilsson T, Nyholm T, Jonsson J, Gunnlaugsson A, Olsson LE. Technical Note: MRI only prostate radiotherapy planning using the statistical decomposition algorithm. Medical Physics. 2015; 42:6090–7. [PubMed: 26429284]

Stanescu T, Hans-Sonke J, Stavrev P, Gino Fallone B. 3T MR-based treatment planning for radiotherapy of brain lesions. Radiology and Oncology. 2006; 40:125–32.

Steenbakkers RJ, Deurloo KE, Nowak PJ, Lebesque JV, van Herk M, Rasch CR. Reduction of dose delivered to the rectum and bulb of the penis using MRI delineation for radiotherapy of the prostate. International Journal of Radiation Oncology* Biology* Physics. 2003; 57:1269–79.

Sun J, Dowling J, Pichler P, Menk F, Rivest-Henault D, Lambert J, Parker J, Arm J, Best L, Martin J, Denham JW, Greer PB. MRI simulation: end-to-end testing for prostate radiation therapy using geometric pelvic MRI phantoms. Physics in Medicine and Biology. 2015; 60:3097–109. [PubMed: 25803177]

Tanderup K, Hellebust TP, Lang S, Granfeldt J, Pötter R, Lindegaard JC, Kirisits C. Consequences of random and systematic reconstruction uncertainties in 3D image based brachytherapy in cervical cancer. Radiotherapy and oncology: journal of the European Society for Therapeutic Radiology and Oncology. 2008; 89:156–63. [PubMed: 18692265]

Tanderup K, Nesvacil N, Pötter R, Kirisits C. Uncertainties in image guided adaptive cervix cancer brachytherapy: impact on planning and prescription. Radiotherapy and oncology: journal of the European Society for Therapeutic Radiology and Oncology. 2013; 107:1–5. [PubMed: 23541642]

Tanderup K, Viswanathan AN, Kirisits C, Frank SJ. Magnetic resonance image guided brachytherapy. Seminars in radiation oncology. 2014; 24:181–91. [PubMed: 24931089]

Tanner SF, Finnigan DJ, Khoo VS, Mayles P, Dearnaley DP, Leach MO. Radiotherapy planning of the pelvis using distortion corrected MR images: the removal of system distortions. Physics in medicine and biology. 2000; 45:2117–32. [PubMed: 10958184]

Tavares WM, Tustumi F, da Costa Leite C, Gamarra LF, Amaro E, Teixeira MJ, Fonoff ET. An image correction protocol to reduce distortion for 3-T stereotactic MRI. Neurosurgery. 2014; 74:121–6. discussion 6–7. [PubMed: 24064479]

Torfeh T, Hammoud R, Perkins G, McGarry M, Aouadi S, Celik A, Hwang K-P, Stancanello J, Petric P, Al-Hammadi N. Characterization of 3D geometric distortion of magnetic resonance imaging scanners commissioned for radiation therapy planning. Magnetic resonance imaging. 2016; 34:645–53. [PubMed: 26795695]

Tsien C, Cao Y, Chenevert T. Clinical applications for diffusion magnetic resonance imaging in radiotherapy. Seminars in radiation oncology. 2014; 24:218–26. [PubMed: 24931097]

Tyagi N, Fontenla S, Zhang J, Cloutier M, Kadbi M, Mechalakos J, Zelefsky M, Deasy J, Hunt M. Dosimetric and workflow evaluation of first commercial synthetic CT software for clinical use in pelvis. Physics in medicine and biology. 2016

Uh J, Merchant TE, Li Y, Li X, Hua C. MRI-based treatment planning with pseudo CT generated through atlas registration. Medical physics. 2014; 41:051711. [PubMed: 24784377]

Ulin K, Urie MM, Cherlow JM. Results of a multi-institutional benchmark test for cranial CT/MR image registration. International Journal of Radiation Oncology* Biology* Physics. 2010; 77:1584–9.

Van Herk M. Errors and margins in radiotherapy. Seminars in radiation oncology. 2004; 14:52–64. [PubMed: 14752733]

van Herk M, Kooy HM. Automatic three-dimensional correlation of CT-CT, CT-MRI, and CT-SPECT using chamfer matching. Medical physics. 1994; 21:1163–78. [PubMed: 7968850]

van Mourik AM, Elkhuizen PH, Minkema D, Duppen JC, Dutch Young Boost Study G. van Vliet-Vroegindeweij C. Multiinstitutional study on target volume delineation variation in breast radiotherapy in the presence of guidelines. Radiotherapy and oncology: journal of the European Society for Therapeutic Radiology and Oncology. 2010; 94:286–91. [PubMed: 20199818]

van Schie MA, Steenbergen P, Dinh CV, Ghobadi G, van Houdt PJ, Pos FJ, Heijmink SW, van der Poel HG, Renisch S, Vik T. Repeatability of dose painting by numbers treatment planning in prostate cancer radiotherapy based on multiparametric magnetic resonance imaging. Physics in Medicine & Biology. 2017; 62:5575. [PubMed: 28557799]

Vorwerk H, Beckmann G, Bremer M, Degen M, Dietl B, Fietkau R, Gsänger T, Hermann RM, Alfred Herrmann MK, Höller U, van Kampen M, Körber W, Maier B, Martin T, Metz M, Richter R, Siekmeyer B, Steder M, Wagner D, Hess CF, Weiss E, Christiansen H. The delineation of target volumes for radiotherapy of lung cancer patients. Radiotherapy and Oncology. 2009; 91:455–60. [PubMed: 19339069]

Wachter S, Wachter-Gerstner N, Bock T, Goldner G, Kovacs G, Fransson A, Potter R. Interobserver comparison of CT and MRI-based prostate apex definition. Clinical relevance for conformal radiotherapy treatment planning. Strahlentherapie und Onkologie: Organ der Deutschen Rontgengesellschaft … [et al]. 2002; 178:263–8.

Wang D, Doddrell D. Geometric Distortion in Structural Magnetic Resonance Imaging. Current Medical Imaging Reviews. 2005; 1:49–60.

Wang H, Balter J, Cao Y. Patient-induced susceptibility effect on geometric distortion of clinical brain MRI for radiation treatment planning on a 3T scanner. Physics in medicine and biology. 2013; 58:465. [PubMed: 23302471]

Wang H, Chandarana H, Block KT, Vahle T, Fenchel M, Das IJ. Dosimetric evaluation of synthetic CT for magnetic resonance-only based radiotherapy planning of lung cancer. Radiat Oncol. 2017; 12:108. [PubMed: 28651599]

Weiss E, Hess CF. The impact of gross tumor volume (GTV) and clinical target volume (CTV) definition on the total accuracy in radiotherapy. Strahlentherapie und Onkologie. 2003; 179:21–30. [PubMed: 12540981]

Weiss E, Richter S, Krauss T, Metzelthin SI, Hille A, Pradier O, Siekmeyer B, Vorwerk H, Hess CF. Conformal radiotherapy planning of cervix carcinoma: differences in the delineation of the clinical target volume: A comparison between gynaecologic and radiation oncologists. Radiotherapy and Oncology. 2003; 67:87–95. [PubMed: 12758244]

Wolterink JM, Dinkla AM, Savenije MHF, Seevinck PR, van den Berg CAT, Išgum I. Deep MR to CT synthesis using unpaired data. Lecture Notes in Computer Science (including subseries Lecture Notes in Artificial Intelligence and Lecture Notes in Bioinformatics). 2017:14–23.

Wyatt J, Dowling JA, Kelly CG, McKenna J, Johnstone E, Speight R, Henry A, Greer PB, McCallum HM. Investigating the generalisation of an atlas-based synthetic-CT algorithm to another centre and MR scanner for prostate MR-only radiotherapy. Phys Med Biol. 2017

Yang Y, Cao M, Kaprealian T, Sheng K, Gao Y, Han F, Gomez C, Santhanam A, Tenn S, Agazaryan N. Accuracy of UTE-MRI-based patient setup for brain cancer radiation therapy. Medical physics. 2016; 43:262–7. [PubMed: 26745919]

Caldwell, Yu H., Balogh, CJ., Mah, K. Toward magnetic resonance-only simulation: segmentation of bone in MR for radiation therapy verification of the head. International journal of radiation oncology, biology, physics. 2014; 89:649–57.

Zaidi H, Montandon ML, Slosman DO. Magnetic resonance imaging-guided attenuation and scatter corrections in three-dimensional brain positron emission tomography. Medical Physics. 2003; 30:937–48. [PubMed: 12773003]

Zheng W, Kim JP, Kadbi M, Movsas B, Chetty IJ, Glide-Hurst CK. Magnetic Resonance–Based Automatic Air Segmentation for Generation of Synthetic Computed Tomography Scans in the Head Region. International Journal of Radiation Oncology* Biology* Physics. 2015; 93:497–506.

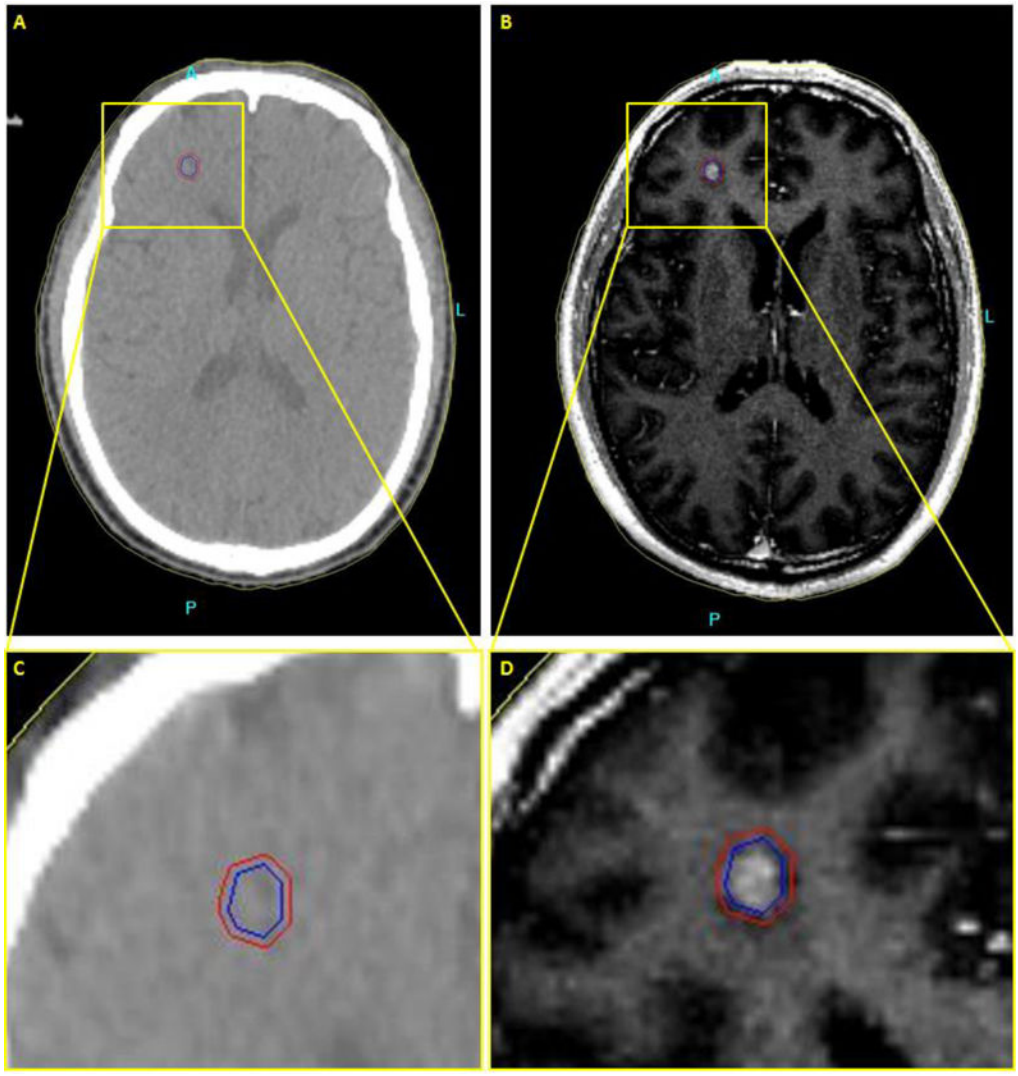

Figure 1.

Axial brain images of patient with a metastatic tumor in the brain. (a,c) CT image. No contrast between the tumor and the surrounding normal tissue. (b,d) T2-weighted Fluid-attenuated inversion recovery image (FLAIR) MR image. Higher soft tissue contrast of the MR image leads to more accurate delineation of the tumor.

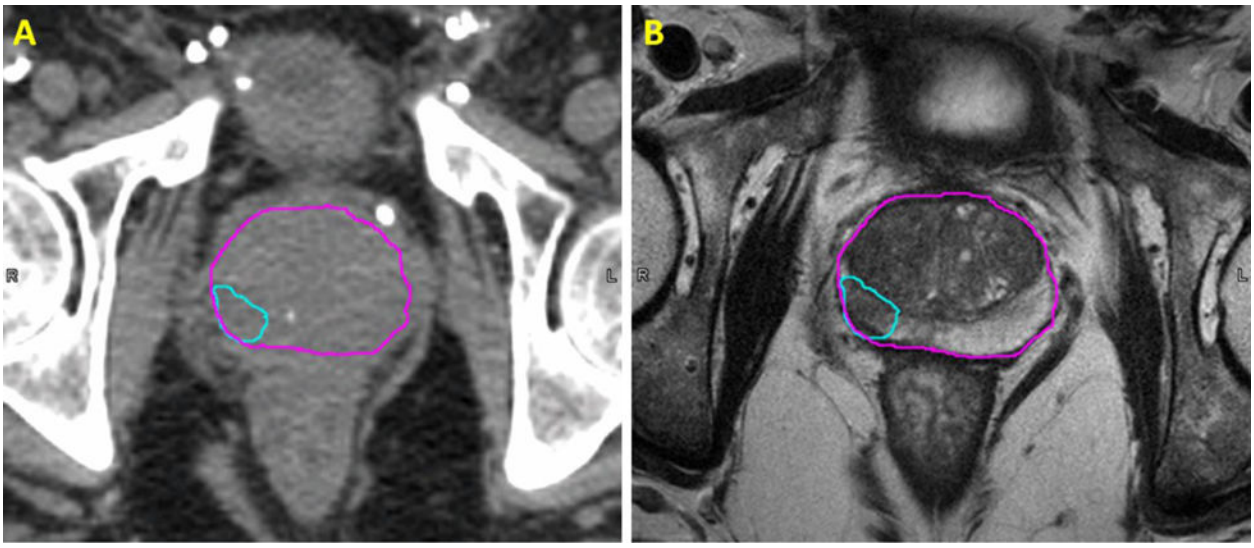

Figure 2.
Comparison of the transverse view of CT (left) and T2-weighted (right) images of a patient with prostate cancer; The volumes are as follows: prostate (magenta) and dominant intraprostatic lesion (cyan).

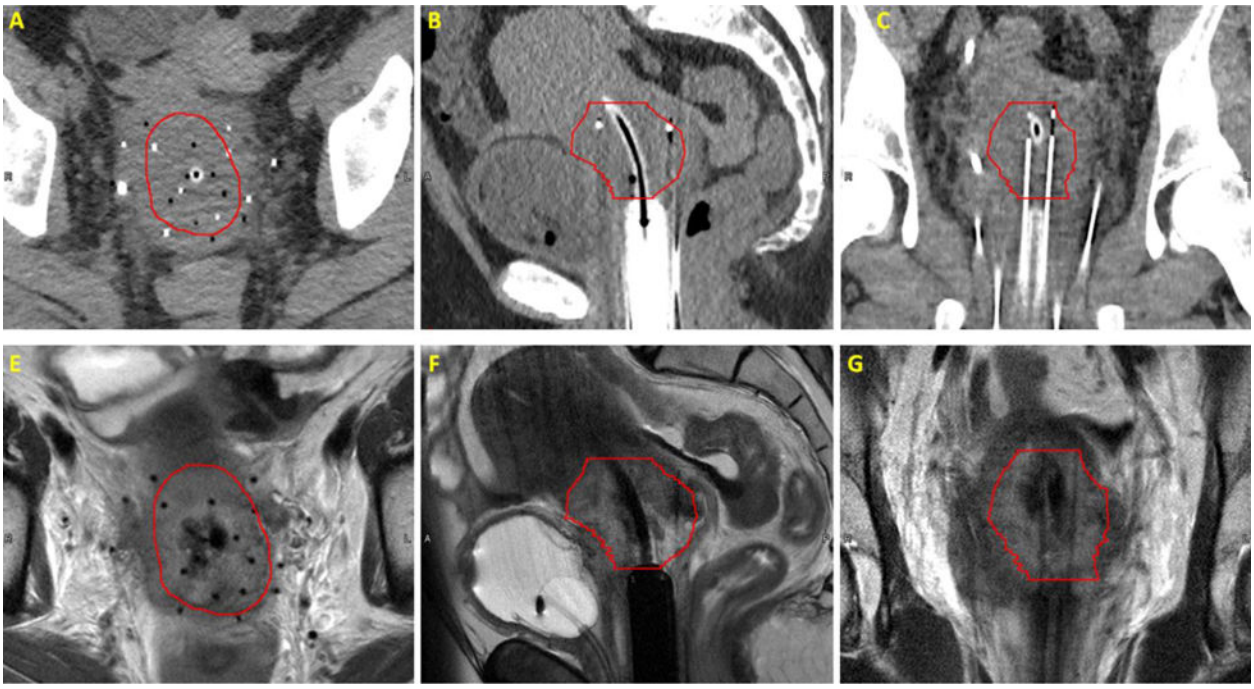

Figure 3.

Comparison of CT and T2-weighted images of a patient with plastic needles and a plastic cylinder and tandem in place; Transverse view of CT (top row) and T2-weighted (bottom row) of a patient's pelvis with axial view showed in left panel and sagittal and coronal views showed in middle and right panels, respectively. High-risk CTV volume shown in red.

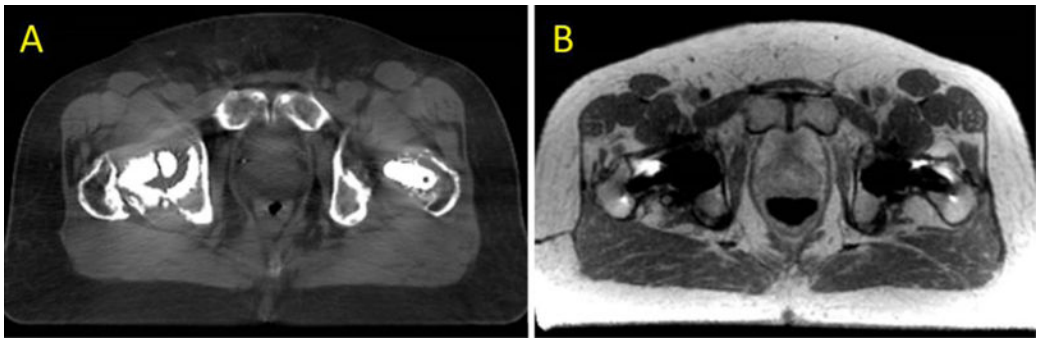

Figure 4.
MAR for CT-SIM (A) and MR-SIM (B) in a prostate cancer patient with bilateral hip implants.

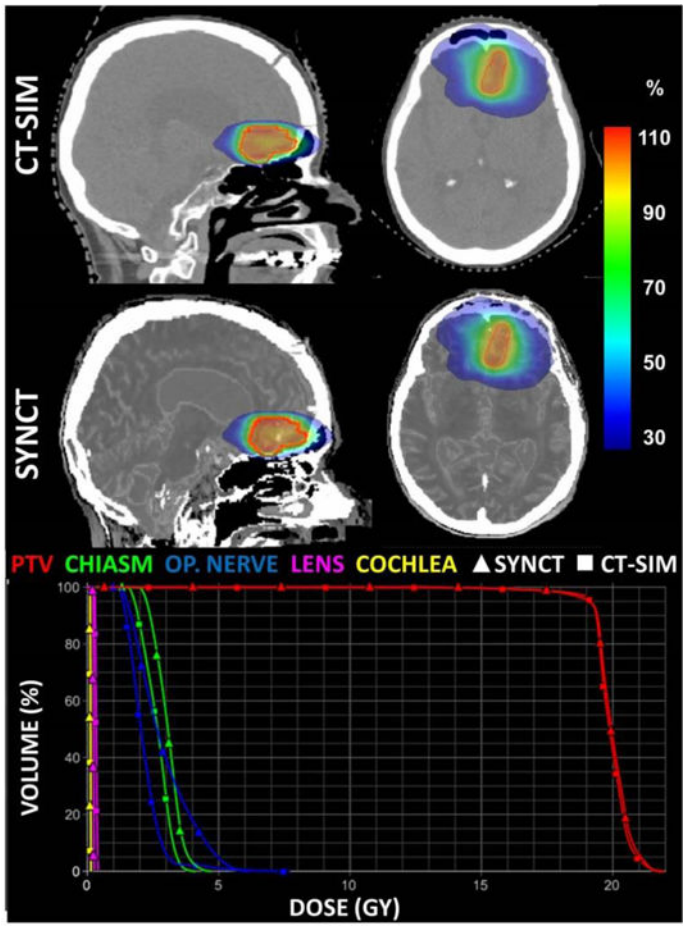

Figure 5.

Treatment planning CT and synthetic CT including dosimetric comparison for an average patient brain cancer patient. Dose planes at isocenter (percent dose) for the CT-SIM and synthetic CT. The corresponding dose histogram is also shown highlighting close agreement between dose calculations for a radiosurgery brain case.

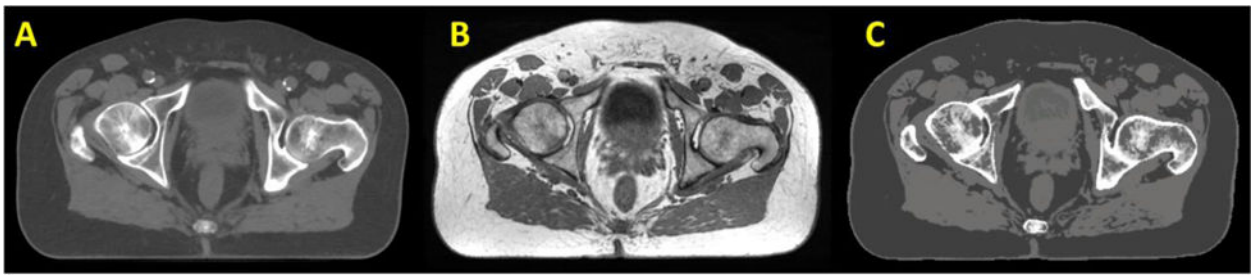

Figure 6.
Transverse view of CT (A), MRI (B) and synthetic CT (C) of a patient's pelvis.

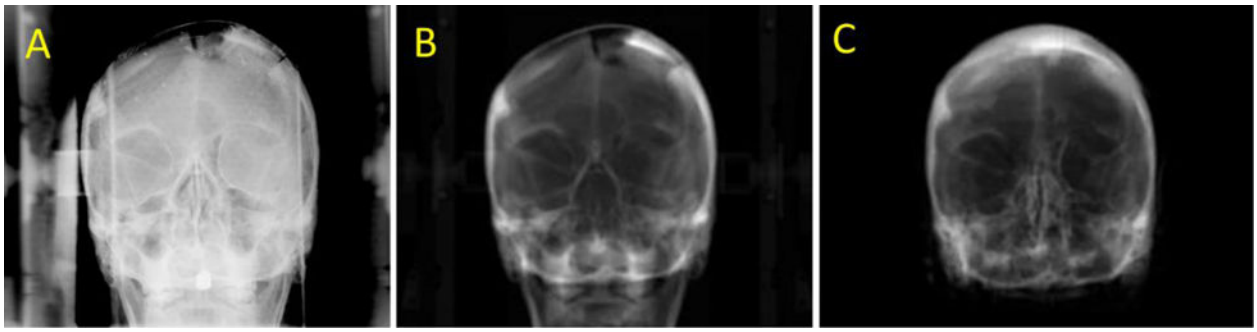

Figure 7.

Anterior kilovoltage planar (A), CT (B), and synthetic CT (C) digitally reconstructed radiographs (DRRs) illustrating that while the skull is well-approximated by the synthetic CT, proper characterization of resection cavities are still a work in progress in the brain.